Table 1 Tip vortex characteristics

Case	U_∞, m/s	Re_c	α, deg	$\Gamma_v/(cU_\infty c_l)$	$-y_c/s$	d/s
1	10	6.8×10^4	5	0.38	0.10	0.15
2	10	6.8×10^4	10	0.41	0.09	0.17
3	15	1.0×10^5	5	0.40	0.10	0.17
4	15	1.0×10^5	10	0.42	0.09	0.14
PIV[7]	25	1.5×10^5	10	0.43	——	0.05

The maximum vortex strength $\Gamma_v/(cU_\infty c_l)$, core location y_c/s, and vortex diameter d/s, listed in Table 1, were extracted from the circulation distributions by fitting hyperbolic tangent curves to the data. The spanwise location where Γ was one-half of its maximum value yielded y_c, and the vortex diameter was the extent between the 5 and 95% circulation values. The experimental uncertainty is 5% for the former two parameters; the vortex diameter uncertainty is much more difficult to quantify because of the asymptotic nature of the curve fit at the two ends.

The normalized maximum vortex strength remains nearly constant (within ±5%) for the four cases considered. The vortex strength of the PIV data shows good agreement with the data at 10 deg, which suggests that the ultrasound method accurately measured the total circulation of the tip vortex. Because of the wandering correction, comparison of the acoustically measured core location with the PIV data would not be appropriate, as indicated in Table 1.

The normalized vortex diameter varied over a range of values and was about three times larger than that from the PIV data. The asymptotic nature of the curve fit at the two extremes makes this parameter very sensitive to small variations in the data. Additionally, the sound pulses had a scale (the diameter of the transducer face) on the order of 2 cm that tends to limit the spatial resolution of the measurements and to result in larger vortex diameters. The vortex diameter based on the maximum tangential velocity reported in Ref. 6 is generally on the order of 10% of the wing span, which corresponds to about 2 cm for our setup. This suggests that the vortex diameter measured in the present experiments was approximately the same size as the sound pulse used to measure the circulation. This is the reason for the larger vortex diameters inferred. The relative spatial resolution of the system would be improved in a larger experimental setup.

Forcing of the vortex was pursued in an attempt to alter the vortex characteristics. The forcing was accomplished by steady and pulsatile injection, as well as suction of air (in the freestream direction) from the vortex core. For the conditions utilized, no changes were found in the forced vortex characteristics over the baseline case at the four-chord measurement location.[9]

Summary

The circulation distribution of a wing tip vortex as a function of the spanwise coordinate was measured directly by an ultrasound technique utilizing a rectangular acoustic path. The vortex was generated by a blunt-ended NACA 0012 half-wing, and the measurements were made at four chords downstream of the trailing edge. The circulation distribution behaved as expected: achieving its highest level when the rectangular integration path completely surrounded the vortex. The circulation decreased rapidly through the vortex center before reaching nearly zero when one side of the integration path traversed through the vortex. The direct acoustic measurements of circulation agreed well with those derived from detailed velocity field data generated by a similar wing. The ultrasound method offers accurate circulation measurements as long as the flow scales are larger than the size of the sound pulse employed in the measurements.

Acknowledgments

The first author was supported by the Massachusetts Space Grant Consortium. We would like to thank M. Gharib of the California Institute of Technology for providing us the PIV data.

References

[1] Johari, H., and Durgin, W. W., "Direct Measurement of Circulation Using Ultrasound," *Experiments in Fluids*, Vol. 25, No. 5/6, 1998, pp. 445–454.

[2] Johari, H., and Moreira, J., "Direct Measurement of Delta-Wing Vortex Circulation," *AIAA Journal*, Vol. 36, No. 12, 1998, pp. 2195–2203.

[3] Corsiglia, V. R., Schwind, R. G., and Chigier, N. A., "Rapid Scanning, Three-Dimensional Hot-Wire Anemometer Surveys of Wing-Tip Vortices," *Journal of Aircraft*, Vol. 10, No. 12, 1973, pp. 752–757.

[4] Baker, G. R., Barker, S. J., Bofah, K. K., and Saffman, P. G., "Laser Anemometer Measurements of Trailing Vortices in Water," *Journal of Fluid Mechanics*, Vol. 65, Pt. 2, 1974, pp. 325–336.

[5] Ciffone, D. L., and Orloff, K. L., "Far-Field Wake Vortex Characteristics of Wings," *Journal of Aircraft*, Vol. 12, No. 5, 1975, pp. 464–470.

[6] Devenport, W. J., Rife, M. C., Liapis, S. I., and Follin, G. J., "The Structure and Development of a Wing-Tip Vortex," *Journal of Fluid Mechanics*, Vol. 312, 1996, pp. 67–106.

[7] Vogt, A., Baumann, P., Gharib, M., and Kompenhans, J., "Investigations of a Wing Tip Vortex in Air by Means of DPIV," AIAA Paper 96-2254, June 1996.

[8] Jacob, J., Savaş, Ö., and Liepmann, D., "Trailing Vortex Wake Growth Characteristics of a High Aspect Ratio Rectangular Airfoil," *AIAA Journal*, Vol. 35, No. 2, 1997, pp. 275–280.

[9] Desabrais, K. J., and Johari, H., "Direct Circulation Measurement of a Wing Tip Vortex Using Ultrasound," AIAA Paper 98-0609, Jan. 1998.

A. Plotkin
Associate Editor

Optimal Structural Control by Substructure Synthesis

M. Sunar*
King Fahd University of Petroleum and Minerals, Dhahran 31261, Saudi Arabia
and
S. S. Rao†
University of Miami, Coral Gables, Florida 33124

Introduction

SUBSTRUCTURAL decomposition techniques have been developed for large flexible structures to reduce the order of their full model to a manageable level. These techniques were applied to the control of large flexible structures by Pan[1] and Sunar and Rao[2] using the linear quadratic regulator control method and by Su et al.[3] using the linear quadratic Gaussian (LQG) control method.

In this Note, a generalized substructural decomposition technique is presented to efficiently design controllers and observers for large flexible structures using the LQG method. The structure is decomposed into substructures and the equations of motion (EOM) are written for all of the substructures. The boundary forces due to subcontrollers of surrounding substructures are included in the EOM as they become available. These EOM are used in the subcontroller and subobserver designs for all of the substructures. The subcontroller and subobserver matrices are assembled to obtain the global controller for the whole structure. The accuracy and efficiency of the substructural technique as compared to the full structural model are numerically illustrated on a large flexible structure.

Substructure Decomposition and Nodal Condensation

Assume that a flexible structure is decomposed into r substructures. The partitioned EOM of any kth substructure in the configuration space with only controller input $\boldsymbol{u}$ can be written as

$$\begin{bmatrix} M_{A_kA_k} & M_{A_kB_k} \\ M_{B_kA_k} & M_{B_kB_k} \end{bmatrix} \begin{Bmatrix} \ddot{\boldsymbol{d}}_{A_k} \\ \ddot{\boldsymbol{d}}_{B_k} \end{Bmatrix} + \begin{bmatrix} C_{d_{A_kA_k}} & C_{d_{A_kB_k}} \\ C_{d_{B_kA_k}} & C_{d_{B_kB_k}} \end{bmatrix} \begin{Bmatrix} \dot{\boldsymbol{d}}_{A_k} \\ \dot{\boldsymbol{d}}_{B_k} \end{Bmatrix} + \begin{bmatrix} K_{A_kA_k} & K_{A_kB_k} \\ K_{B_kA_k} & K_{B_kB_k} \end{bmatrix} \begin{Bmatrix} \boldsymbol{d}_{A_k} \\ \boldsymbol{d}_{B_k} \end{Bmatrix} = \begin{bmatrix} D_{A_kA_k} & D_{A_kB_k} \\ D_{B_kA_k} & D_{B_kB_k} \end{bmatrix} \begin{Bmatrix} \boldsymbol{u}_{A_k} \\ \boldsymbol{u}_{B_k} \end{Bmatrix} \quad (1)$$

Received 14 April 2000; accepted for publication 27 July 2000.

*Assistant Professor, Mechanical Engineering Department.
†Professor and Chairman, Department of Mechanical Engineering.

where M, C_d, K, and D are the mass, damping, stiffness, and controller input matrices, and $\boldsymbol{d}$ is the displacement vector. In Eq. (1), the subscripts A_k and B_k denote the internal and boundary degrees of freedom (DOF) for the kth substructure, respectively. The internal and boundary DOF of a substructure will depend on the surrounding substructure considered. For example, assume that the kth substructure has s surrounding substructures and its original internal DOF is I_k and that the boundary DOF between the kth substructure and its $(k+1)$th surrounding substructure is B_{1k}. Then the sets of the internal and boundary DOF for the kth substructure with respect to its $(k+1)$th surrounding substructure are given as $\{A_k\} = \{I_k, B_{2k}, B_{3k}, \ldots, B_{sk}\}$ and $\{B_k\} = \{B_{1k}\}$.

The Guyan condensation scheme is used to condense and, hence, to include the effects of the internal DOF on the boundary DOF. This scheme may be justified when the frequencies of the applied force are small compared to the natural frequencies of the structure or the entries of M_{AA} and M_{AB} are much smaller then those of K_{AA} and K_{AB}. According to the Guyan scheme, the following transformation is carried out:

$$\begin{Bmatrix} \boldsymbol{d}_{A_k} \\ \boldsymbol{d}_{B_k} \end{Bmatrix} = \begin{bmatrix} -K_{A_kA_k}^{-1} K_{A_kB_k} \\ I_{B_k} \end{bmatrix} \boldsymbol{d}_{B_k} = T_k \boldsymbol{d}_{B_k} \tag{2}$$

Controller and Observer Designs by Substructural Decomposition

The iterative substructural scheme for general flexible structures using the LQG control method is outlined in this section. The model of the kth substructure in state space is given as

$$\dot{\boldsymbol{x}}_k = \left[A_k + \bar{F}_{B_k}\right]\boldsymbol{x}_k + B_k\boldsymbol{u}_k + \boldsymbol{w}_k = \bar{A}_k\boldsymbol{x}_k + B_k\boldsymbol{u}_k + E_k\boldsymbol{w}_k$$

$$\boldsymbol{y}_k = C_k\boldsymbol{x}_k + \boldsymbol{v}_k \tag{3}$$

where

$$\boldsymbol{x}_k = \begin{bmatrix} \boldsymbol{d}_{A_k} \\ \boldsymbol{d}_{B_k} \\ \dot{\boldsymbol{d}}_{A_k} \\ \dot{\boldsymbol{d}}_{B_k} \end{bmatrix}^T, \qquad \bar{F}_{B_k}\boldsymbol{x}_k = \sum_{i=1}^{s} \begin{Bmatrix} 0 \\ M_k^{-1}\boldsymbol{F}_{B_{ik}} \end{Bmatrix}$$

$$A_k = \begin{bmatrix} 0 & I \\ -M_k^{-1}K_k & -M_k^{-1}C_{d_k} \end{bmatrix}, \qquad B_k = \begin{bmatrix} 0 \\ M_k^{-1}D_k \end{bmatrix} \tag{4}$$

In the preceding equations, $\boldsymbol{F}_{B_{ik}}$ is the controller force vector generated by the ith surrounding substructure of the kth substructure in the preceding iteration, E is the noise matrix, and $\boldsymbol{w}$ and $\boldsymbol{v}$ are the noise vectors due to dynamics and measurement, respectively. The subcontroller for the kth substructure is designed using the feedback control law as

$$\boldsymbol{u}_k = -K_{c_k}\boldsymbol{x}_{ok} = -R_k^{-1}B_k^T P_{c_k}\boldsymbol{x}_{ok} \tag{5}$$

where $\boldsymbol{x}_{ok}$ is the observed state vector and P_{c_k} satisfies the ARE

$$\bar{A}_k^T P_{c_k} + P_{c_k}\bar{A}_k - P_{c_k}B_kR_k^{-1}B_k^T P_{c_k} + Q_k = 0 \tag{6}$$

The subobserver is designed using the Kalman filter matrix as

$$K_{f_k} = P_{f_k}C_k^T V_k^{-1} \tag{7}$$

where P_{f_k} satisfies

$$P_{f_k}\bar{A}_k^T + \bar{A}_kP_{f_k} - P_{f_k}C_k^T V_k^{-1}C_kP_{f_k} + W_k = 0 \tag{8}$$

The subcontroller force generated within the kth substructure, $\boldsymbol{f}_k$, is found using Eq. (5) as

$$\boldsymbol{f}_k = D_k\boldsymbol{u}_k = -D_kK_{c_k}\boldsymbol{x}_{ok} = -D_kK_{c_k}\begin{Bmatrix} \boldsymbol{d}_{A_k} \\ \boldsymbol{d}_{B_k} \\ \dot{\boldsymbol{d}}_{A_k} \\ \dot{\boldsymbol{d}}_{B_k} \end{Bmatrix}_o \tag{9}$$

which is rewritten via the condensation scheme of Eq. (2) as

$$\boldsymbol{f}_k = -D_kK_{c_k}\bar{T}_k\begin{Bmatrix} \boldsymbol{d}_{B_k} \\ \dot{\boldsymbol{d}}_{B_k} \end{Bmatrix}_o \tag{10}$$

where

$$\bar{T}_k = \begin{bmatrix} T_k & 0 \\ 0 & T_k \end{bmatrix} \tag{11}$$

Solution Procedure

The basic steps of the technique are summarized as follows. 1) A flexible structure is decomposed into r substructures. 2) The substructures are numbered from 1 to r. In the first iteration, the subcontroller and subobserver are designed for the first substructure assuming no boundary forces due to subcontrollers of surrounding substructures. The boundary forces due the subcontroller of the first substructure are condensed to the boundary DOF of its surrounding substructures. Subcontroller and subobserver designs for the remaining substructures are carried out with the inclusion of subcontroller forces condensed to the boundary DOF from preceding substructures. 3) After designing the subcontrollers and subobservers for all of the substructures, they are assembled to obtain the global controller and observer matrices K_c and K_f for the whole structure. The eigenvalues of $A - BK_c$ and $A - K_fC$ are computed. Here A, B, and C denote the state and controller input and output matrices of the whole structure. 4) Iterations are terminated when these closed-loop eigenvalues cease changing considerably. The termination is due to better representation of the subcontroller forces as the iterations progress.

Case Study and Remarks

A large flexible-structure, 45-bar truss, shown in Fig. 1, is taken as an example to illustrate the proposed substructural decomposition

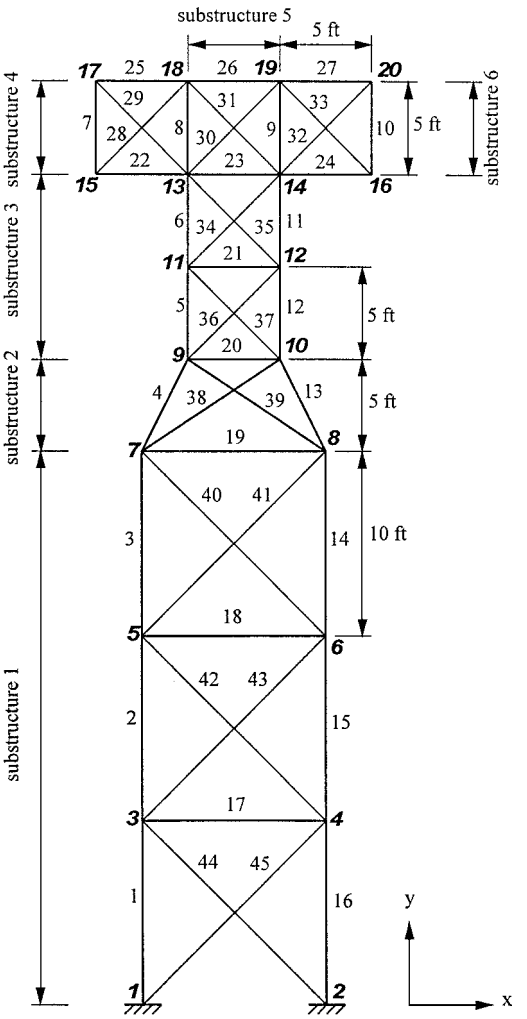

Fig. 1 Flexible 45-bar truss.

technique. The truss is made of aluminum with Young's modulus of $E = 10^7$ psi and mass density of $\rho = 0.1$ lb/in^3. The cross-sectional areas of all of the members are taken as 2 in^2. The dimensions of the structure are indicated in Fig. 1. The actuators and displacement sensors are collocated in nodes 7–10, 13, 14, 18, and 19. The actuators can generate forces in the x and y directions at these nodes. For the LQG control method, it is assumed that $Q = 10^3 \times I_Q$, $R = I_R$, $W = 10^5 \times I_W$, and $V = 10^{-6} \times I_V$, where I_Q, I_R, I_W, and I_V are the identity matrices with appropriate dimensions. For the observer design, the control inputs from the actuators are taken as noise inputs to make the structure robust to parameter changes at the control inputs.

The structure is decomposed into six substructures as shown in Fig. 1. The members at the boundaries are shared by the neighboring substructures. Sharing means that these members are kept in each corresponding substructure with cross-sectional areas taken as 1 in^2. The sensor/actuator pairs at the boundaries are included in the feedback and observer designs of all of the sharing substructures. This poses no implementation problems because the proposed scheme is to be applied globally once the feedback and observer designs are completed from the substructure level.

The execution times (user plus system on Unix) recorded on an IBM RS-6000 machine for the feedback design using the complete and substructural models are listed as 37.53 and 5.65 s and for the observer design as 29.42 and 3.22 s, respectively. The closed-loop structural responses due to a unit step disturbance force acting at node 20 in the $-y$ direction are found using both complete and substructural models of the structure, and two are shown in Figs. 2 and 3. Figures 4 and 5 are the Bode-magnitude plots of the open-loop structure and closed-loop structure via complete and substructural models. Bode-phase plots show the same trend. It is evident from Figs. 2–5 that the results of the substructural decomposition technique are in good agreement with those of the complete model. The Bode plot in the x direction (Fig. 4) indicates some discrepancy between the complete and substructural models at high frequencies, which is expected due to the Guyan condensation scheme.

For the comparison of the closed-loop eigenvalues, an error parameter is defined as

$$e = 100 \times |d_s - d_w|/d_s \tag{12}$$

where d_s and d_w are the distances of the eigenvalues from the origin for the substructural and complete models, respectively. For the feedback eigenvalues, that is, those of $A - BK_c$, the average and maximum e are noted as 0.03 and 0.86, respectively. For the observer eigenvalues, that is, those of $A - K_f C$, the average e is computed as 2.71, whereas the eigenvalues of $-255.2 \pm 240.1j$ (substructural) and $-123.3 \pm 191.8j$ (complete) result in the maximum $e = 34.92$.

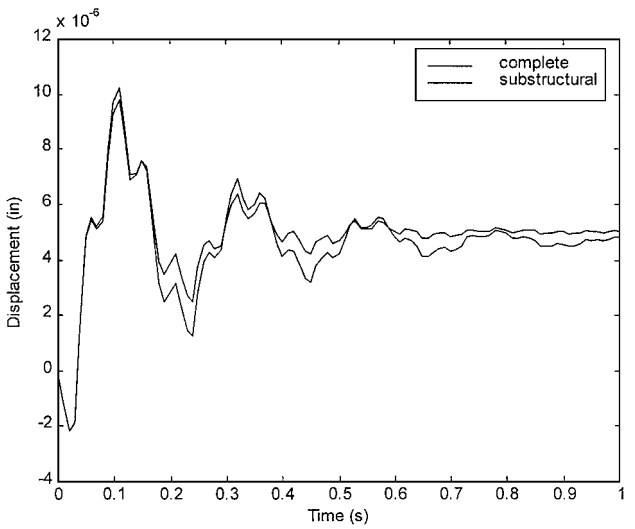

Fig. 2 Closed-loop displacement of the structure at node 9 in x direction.

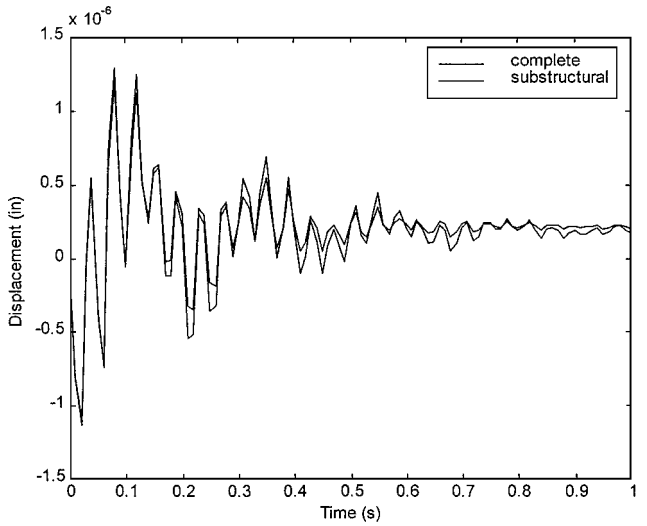

Fig. 3 Closed-loop displacement of the structure at node 9 in y direction.

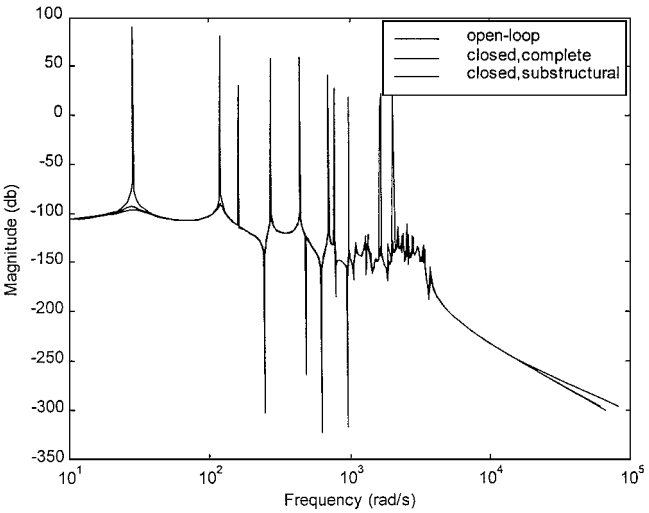

Fig. 4 Bode-magnitude plot of the structure: output is at node 9 in x direction.

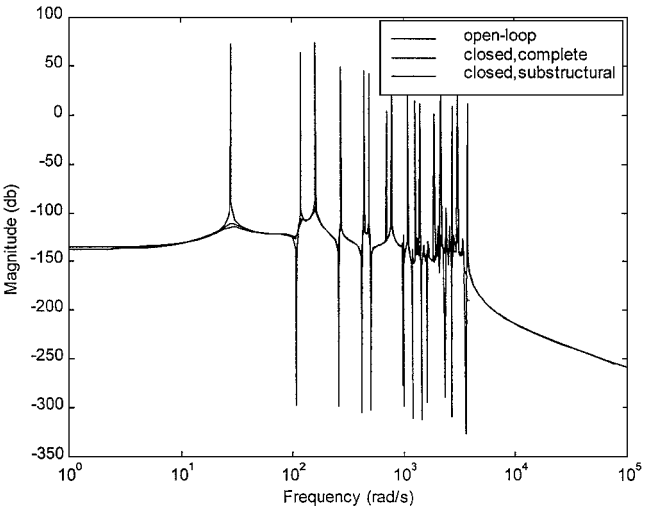

Fig. 5 Bode-magnitude plot of the structure: output is at node 9 in y direction.

In general, the substructural scheme pushes the real parts of the eigenvalues farther left in the complex plane.

Conclusions

The numerical results indicate the overall accuracy and numerical efficiency of the substructural control technique as compared to the LQG design by the complete model. The proposed method in general assumes no restrictions on the types of substructures and on the locations of sensors and actuators.

Acknowledgment

The first author gratefully acknowledges the support of King Fahd University of Petroleum and Minerals in carrying out this research.

References

[1]Pan, T. S., "Robust Structural and Control Design for Flexible Structures," Ph.D. Dissertation, Purdue Univ., West Lafayette, IN, Dec. 1989, Chap. 2.

[2]Sunar, M., and Rao, S. S., "Substructure Decomposition Method for the Control Design of Large Flexible Structures," *AIAA Journal*, Vol. 30, No. 10, 1992, pp. 2573–2575.

[3]Su, T.-J., Babuska, V., and Craig, R. R., Jr., "Substructure-Based Controller Design Method for Flexible Structures," *Journal of Guidance, Control, and Dynamics*, Vol. 18, No. 5, 1995, pp. 1053–1061.

A. M. Waas
Associate Editor

Fracture Mechanics of Mode Separation Based on Beam Theory

R. K. Pandey*
General Electric Corporate Research and Development, Niskayuna, New York 12309

Introduction

LAMINATED structures are finding increasing applications in a wide range of industrial and consumer products such as printed circuit boards, aircrafts, ships, automobiles, sporting goods, etc. Quite often these structures delaminate during service conditions, causing a change in the part performance. Estimation of the part performance using analytical methods is very complex and, hence, is currently evaluated using cumbersome two- or three-dimensional numerical techniques. Unfortunately, these numerical methods are time consuming and computationally very expensive. This has led to a search for a simplistic model that can be used for solving these types of fracture mechanics problems efficiently, thereby reducing the design cost and cycle time. Based on the loading and geometry, a typical delamination is driven by a mix mode fracture. Evaluation of the effect of these delaminations on the structural performance requires separation of the strain energy release rate into its mode I and mode II components.

Suo and Huchinson[1] developed an analytical model to calculate the strain energy release rate for a crack at the interface of two homogeneous layers. Parameters used for separating the strain energy release rate into mode I and II strain energy release rates are obtained through numerical analysis. A crack in a single homogeneous structure is a special case of the model. Schapery and Davidson[2] used classical plate theory for predicting the strain energy release rate and for separating it into its constituents for a cracked plate. However, all of the four parameters needed for the mode separation could not be obtained from the plate theory and the determination of at least one of the parameters required numerical analysis.

Williams[3] proposed a mode separation method using the assumption that the mode II fracture causes identical curvatures in two split segments of a double cantilever beam. However, this assumption provides satisfactory results only for a few trivial cases as discussed in detail by Sun and Pandey.[4] Suo[5] and Nilsson and Storakers[6] also separately proposed new methods for mode separation using classical theories. In most of the cases discussed here, parameters used for the mode separation are either unknown or known only for a few special cases.

Separation of a strain energy release rate into its modes, especially those lying at the interfaces, is complex. In the present work, a method for separating the strain energy release rate for a homogeneous isotropic cracked beamlike structure, as shown in Fig. 1, is studied. The proposed method assumes that equal transverse displacement of the split segments near the crack tip causes mode II fracture and applies analytically obtained crack-tip compliance[4] for separating the modes.

Problem Statement

Consider a cracked homogeneous isotropic beam shown in Fig. 1. The beam has a crack of length a, the thicknesses of the upper and the lower segments of the beam are h_t and h_b, and the moments acting on these segments are M_t and M_b, respectively. Under the action of the moments just defined, assume that the beam experiences mixed mode fracture, that is, the strain energy release rate has both mode I and mode II components. The total strain energy release rate for the described structure under pure moment loading can be accurately expressed as[4]

$$G = \frac{M_t^2}{2EI_t} + \frac{M_b^2}{2EI_b} - \frac{(M_t + M_b)^2}{2EI_0} \tag{1}$$

where E is the elastic modulus of the material and I is the moment of inertia of different segments of the beam identified by their subscripts; subscript 0 stands for unsplit segment. In the present work, a method is proposed to separate G into its mode I and II components (G_{I} and G_{II}) using the elasticity solution of the near tip compliance and the definition of the virtual crack closure method of strain energy release rate calculation.

Solution Approach

Consider the beam shown in Fig. 1a under a general set of moment loads. The equivalent moments on the near tip cross section are M_t and M_b, which can be considered to be made of two sets of moments as shown in Fig. 1b, one causing mode I fracture and the other causing mode II fracture. Let M_{I} and αM_{I} be the moments

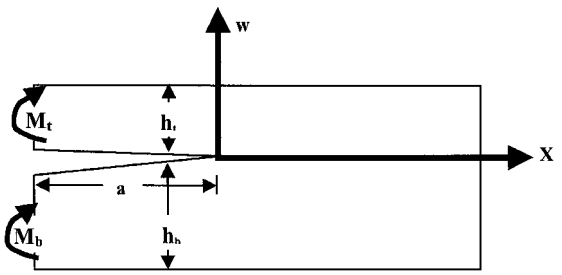

Fig. 1a Cracked beam under moment loading.

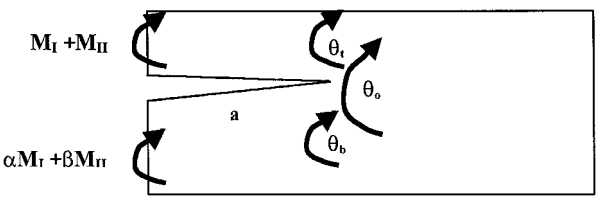

Fig. 1b Equivalent mode I and mode II moment components.

Received 16 January 2000; revision received 10 July 2000; accepted for publication 19 July 2000.

*Senior Staff Engineer, 1 Research Circle; currently Team Leader, TECO–Westinghouse Motor Company, 5100 N. IH 35, Round Rock, TX 78681; pandeyr@teco-wmc.com.